A study of the stress ratio effects on fatigue crack growth using the unified two-parameter fatigue crack growth driving force

A.H. Noroozi, G. Glinka *, S. Lambert

University of Waterloo, Department of Mechanical Engineering, Waterloo, Ont., Canada N2L 3G1

Abstract

A unified two-parameter fatigue crack growth driving force model was developed to account for the residual stress and subsequently the stress ratio effect on fatigue crack growth. It was found that the driving force should be expressed as a combination of the maximum stress intensity factor, K_{max}, and the stress intensity range, ΔK, corrected for the presence of the residual stress. As a result, the effects of residual stresses manifest themselves in changes of the applied maximum stress intensity factor and the applied stress intensity range. A two-parameter function of the maximum total stress intensity factor, $K_{max,tot}$, and the total stress intensity range, ΔK_{tot}, was proposed to model the fatigue crack growth rate data obtained at various R-ratios. Based on the analysis, the unified two-parameter driving force, $\Delta \kappa = K_{max,tot}^{p} \Delta K_{tot}^{(1-p)}$, was derived accounting for the mean stress or the stress ratio effect on fatigue crack propagation. It was shown that the two-parameter driving force, $\Delta \kappa = K_{max,tot}^{p} \Delta K_{tot}^{0.5}$, was capable of correlating fatigue crack growth data obtained under a wide range of load ratios and fatigue crack growth rates spanning from the near threshold to the high growth rate regime.

The model was successfully verified using a wide range of fatigue crack growth data obtained for Al 2024-T351 aluminium alloy, St-4340 steel alloy and Ti–6Al–4V titanium alloy with load ratios, R, ranging from −1 to 0.7.
© 2007 Elsevier Ltd. All rights reserved.

Keywords: Fatigue crack growth; Stress intensity factor; R-ratio; Two-parameter driving force; Residual stress

1. Introduction

Throughout their service life, machines, equipment, vehicles, buildings and aircraft are subjected to loads, the majority of which fluctuates with time. This kind of loading causes small cracks to grow during the life of a component and leads to fatigue failure. The cracks either pre-existed at the time of manufacturing or were created by in-service conditions. Therefore, the growth of the crack should be predictable to provide guidelines for inspection programs, which ensure that cracks will never propagate and fail prior to detection. Therefore, fatigue crack growth prediction models must be developed.

During the last four decades, a lot of research effort has focused on fatigue crack growth and prediction models. The most successful and popular model has been Paris' law [1] based on the applied stress intensity range, ΔK_{appl}, as the only governing parameter for fatigue crack growth. The Paris equation prompted widespread research aiming at possible improvements of its original form and at the analytical modeling of fatigue crack growth, in general. One of the fundamental problems concerning the Paris expression is the quantification of the mean stress effect. In other words, the apparent effectiveness of the applied stress intensity range, ΔK_{appl}, is influenced by the load ratio R (minimum load/maximum load).

In 1971, Elber [2] modified the applied stress intensity factor range, ΔK_{appl}, introducing a closure mechanism in order to characterize the effect of load ratio, R, on fatigue crack growth. The contemporary belief is that the crack tip closure concept can explain mean stress effects on the

* Corresponding author. Tel.: +1 519 888 4567x33339; fax: +1 519 888 6197.

E-mail address: gggreg@mecheng1.uwaterloo.ca (G. Glinka).

Nomenclature

a	crack length	$K_{max,appl}$	maximum applied stress intensity factor
b	fatigue strength exponent	$K_{min,appl}$	minimum applied stress intensity factor
c	fatigue ductility exponent	ΔK_{appl}	applied stress intensity range
C	fatigue crack growth constant	$K_{max,net}$	maximum net stress intensity factor
D	fatigue damage	$K_{min,net}$	minimum net stress intensity factor
E	modulus of elasticity	ΔK_{net}	net stress intensity range
K'	cyclic strength coefficient	$K_{max,tot}$	total maximum stress intensity factor
M_1, M_2, M_3	weight function parameters	$K_{min,tot}$	total minimum stress intensity factor
$m(x,a)$	weight function	ΔK_{tot}	total stress intensity range
N	number of cycle	$\Delta\kappa$	two parameter driving force
P	the unit point force	$K_{max,th}$	maximum threshold stress intensity factor
n'	cyclic strain hardening exponent		
p	driving force constant	ΔK_{th}	threshold stress intensity range
R	stress ratio	$S_{max,appl}$	maximum applied nominal (remote) stress
R_{appl}	applied stress ratio		
x	distance from the crack tip	$S_{min,appl}$	minimum applied nominal (remote) stress
Y	geometrical stress intensity correction factor		
		ΔS_{appl}	applied nominal (remote) stress range
da/dN	crack growth rate	$\sigma_r(x)$	residual stress distribution
FCG	fatigue crack growth	σ_{max}	maximum stress ahead of the crack tip
SIF	stress intensity factor	$\tilde{\sigma}_{max}^a$	maximum actual stress over the first elementary block
SWT	Smith-Watson-Topper fatigue damage parameter		
		$\Delta\tilde{\sigma}^a$	actual stress range over the first elementary block
γ	fatigue crack growth equation exponent	$\tilde{\sigma}_{max,net}^e$	maximum net pseudo-elastic stress over the first elementary block
ρ^*	notch tip radius or elementary material block size	$\tilde{\sigma}_{min,net}^e$	minimum net pseudo-elastic stress over the first elementary block
v	Poisson's coefficient	$\Delta\tilde{\sigma}_{net}^e$	net elastic stress range over the first elementary block
σ_f'	fatigue strength coefficient		
ε_f'	fatigue ductility coefficient	$\Delta\sigma_{th}$	threshold stress range
$\tilde{\varepsilon}_{max}^a$	maximum actual strain over the first elementary block	$\Delta\tilde{\sigma}_{th}^a$	actual threshold stress range over the first elementary block
$\Delta\tilde{\varepsilon}^a$	actual strain range over the first elementary block	$\Psi_{y,i}$	the averaging constant corresponding to the i-th elementary block, $\Psi_{y,1} = 1.633$, $\Psi_{y,2} = 0.8967$, $\Psi_{y,3} = 0.6773$, $\Psi_{y,4} = 0.5641$
$\Delta\varepsilon$	strain range ahead of the crack tip		
K	stress intensity factor		
K_r	residual stress intensity factor		

fatigue crack growth. However, mounting evidence suggests that this may not be true; the model was difficult to use, required experimental calibrations and was not systematic [3–7]. Experimental results indicate that the crack-opening load, P_{op}, depends on the measurement location relative to the crack tip and the technique employed [3,4]. Generally, measurements taken at points far away from the crack tip give lower opening loads compared to measurements taken close to the crack tip. In a vacuum test, where closure is absent, the fatigue crack growth (FCG) should be faster than in the air test, but experimental results contradict such a belief [5]. Recently, Kujawski, [6] Donald and Paris [7] observed that by using the crack closure model fatigue crack growth curves cannot be correlated in the near threshold regime for aluminum alloys.

Therefore, fatigue researches have attempted [6–10] to use alternative methods, for example by assuming a two-parameter driving force combining the applied maximum stress intensity factor, $K_{max,appl}$, and the applied stress intensity range, ΔK_{appl}, in order to analyze the fatigue crack growth behavior. The two-parameter driving forces are capable of explaining the R-ratio effect on fatigue crack growth behavior. However, the available two-parameter driving force models [6–9] tend to be suitable for only high stress ratios. In general, they cannot explain the influence of the compressive part of the load history on fatigue crack growth. In addition, the primary two-parameter models were strictly empirical.

It is generally accepted that fatigue crack growth depends on local stresses and strains at the crack tip.

So far, none of the prediction models can account for the effect of local stresses and strains on fatigue crack growth. Therefore, the unified two-parameter model has been proposed to account for the effect of crack tip local stresses and strains on fatigue crack growth. The model also accounts for the mean stress effect based on the analysis of the elastic–plastic strain–stress history at the crack tip.

2. Formulation of the unified two-parameter fatigue crack growth model

2.1. Description of the proposed model

After the development of fracture mechanics in 1960, the stress intensity factor range was proposed to use as a parameter characterizing the fatigue crack growth. However, it was later found out that FCG was controlled not only by the stress intensity factor range but also by the maximum stress intensity factor. In spite of the fact that the local stresses and strains near the crack tip are dominant factors as far as the FCG is concerned, there has been little effort to establish a quantitative link between them and the applied stress intensity factors. Recently, Noroozi et al. [11] have formulated a unified two-parameter model to correlate the maximum stress intensity factor and the stress intensity range with the actual elasto-plastic crack tip stress–strain field. It was also necessary to address the fact that the actual correlation was significantly influenced

by the residual stress induced at the crack tip by the cyclic plastic deformation.

During the first loading reversal or the first nominal stress reversal from 0 to 1 (Fig. 1a), the material near the crack tip is deformed plastically forming a monotonic plastic zone as shown in Fig. 1c. During the un-loading part of the cycle (paths 1–5 in Fig. 1a) the crack tip deformations are smaller than those created during the previous loading reversal. Thus, the plastic zone created during loading cannot disappear and a small portion of the plastic zone is deformed again in the reversed direction. This re-deformed part of the plastic zone is called the cyclic plastic zone (see Fig. 1c and load level 5). This plastically deformed material is left at the crack tip like an obstacle for subsequent reversals. The plastically deformed material prevents the region behind the crack tip from being closed. In other words, the fatigue crack surfaces do come into contact with each other but not just behind the crack tip, even if compressive loads are applied. This phenomenon was found experimentally and numerically by Bowels [12], Zhang [13], Sander and Richard [14], and also by the finite element analyses carried out by Pommier [15]. The effect of the plastic zone presence resulting in the lack of contact behind the crack tip can be modeled by taking into account the crack tip residual stress. The crack opening behind the tip is modeled by adding the hypothetical symmetrical residual stress distribution behind the crack tip analogous to that one existing ahead of the crack tip (Fig. 2). By representing the residual
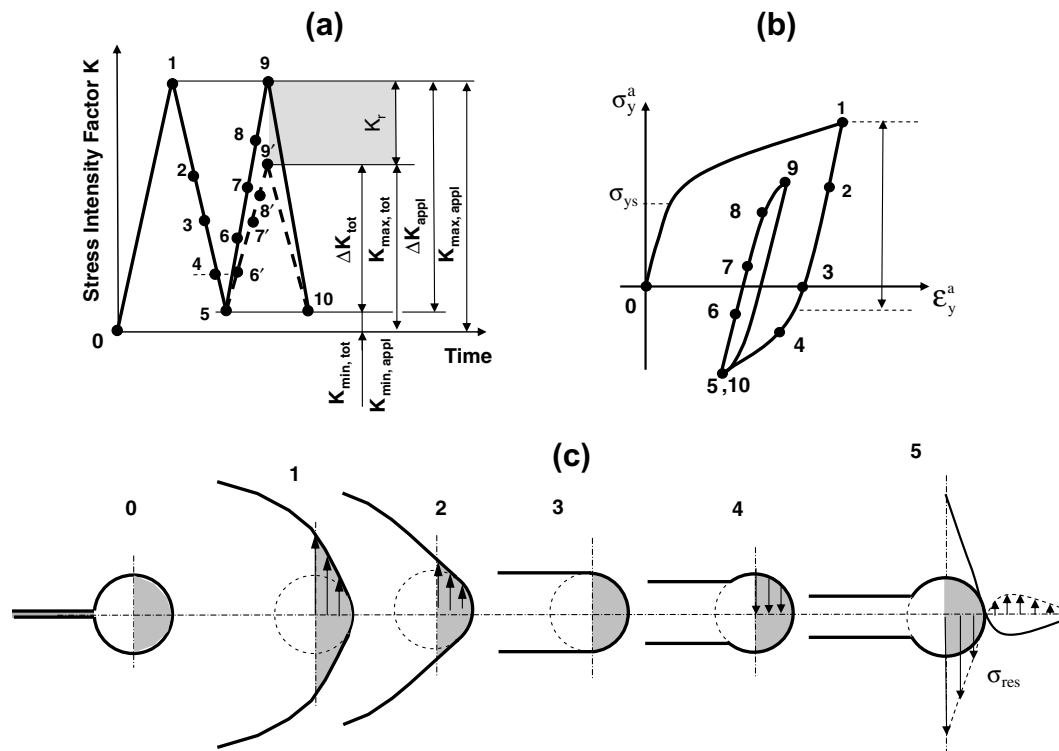

Fig. 1. Schematic crack tip geometry and displacement field, cyclic plastic zone, crack tip stress–strain response and the residual stress distribution: (a) applied load (stress intensity factor) history, (b) qualitative stress–strain response at crack tip, and (c) evolution of the crack opening displacements in the crack tip region.
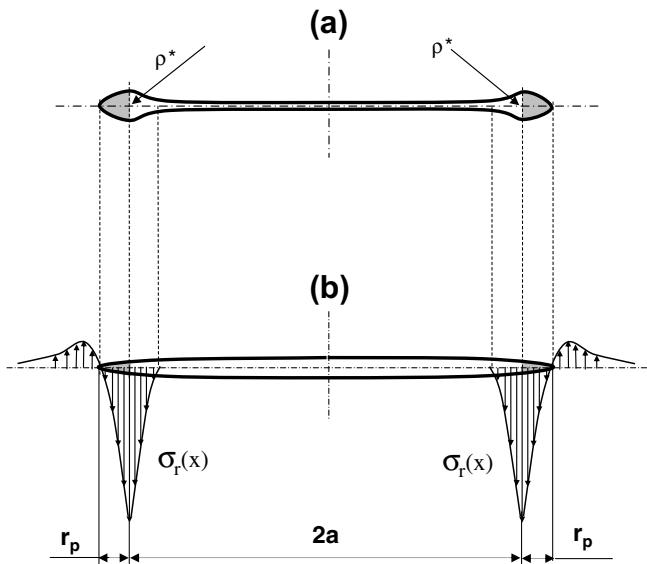
Fig. 2. Approximate crack tip displacement field and corresponding residual stress distribution: (a) illustration of the displacement field around the plastic zone, and (b) residual stress distribution required for generating the displacement field.

stress in terms of the residual stress intensity factor, K_r, the effect of the residual crack tip stress–strain field can be quantified in terms of the residual stress intensity factor, K_r. In order to calculate the residual stress intensity factor, K_r, it is necessary to determine the elasto-plastic material stress–strain response at the crack tip. The expected stress–strain response at the crack tip is shown schematically in Fig. 1b. The residual stress at the crack tip is induced by the first two reversals (0–1 and 1–5 in Fig. 1a). Because of the residual stress created by the first

two reversals, the maximum stress at the crack tip corresponding to the maximum load at the end of the third reversal (at point 9 in Fig. 1a) cannot reach the same level as that one at the end of the first loading reversal (at point 1 in Fig. 1a). This effect can be modeled by using the resultant maximum stress intensity factor, $K_{max,tot}$, obtained by decreasing the applied maximum stress intensity factor, $K_{max,appl}$, by the residual stress intensity factor, K_r. It is assumed that the minimum stress intensity factor is not affected by the crack tip residual stress. As a result of such a correction, both the resultant maximum stress intensity factor, $K_{max,tot}$, and the resultant stress intensity range, ΔK_{tot}, are affected by the plasticity-induced crack tip residual stresses.

2.2. Basics of the proposed model

The proposed unified two-parameter FCG model is based on the following assumptions [11] and computational techniques:

- The material is composed of elementary particles of a finite dimension ρ^*. It represents an elementary material block size, below which material cannot be regarded as a continuum, Fig. 3a.
- The fatigue crack is regarded as a notch with the tip radius ρ^*.
- The macroscopic material properties used in the model are the Ramberg–Osgood cyclic stress–strain curve [16] and the Manson–Coffin strain–life fatigue curve [17].
- The fatigue crack growth is considered as successive crack increments due to crack re-initiations over the distance ρ^*.
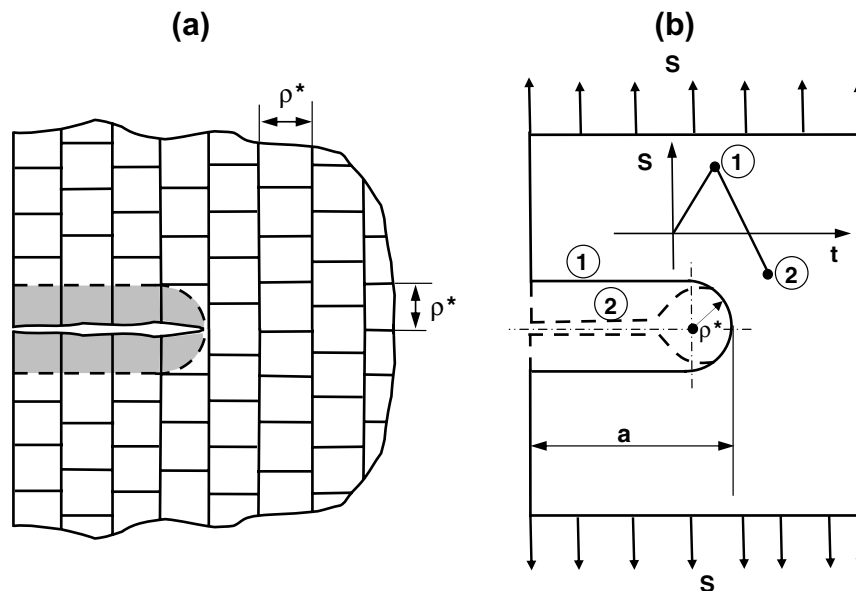

Fig. 3. The discrete material model and the crack tip geometry at the maximum and minimum load: (a) crack and the discrete elementary material blocks. (b) The crack model at the tensile maximum and compressive minimum loads used for the linear elastic stress analysis.

- The number of cycles "N" necessary to fail the material over the distance ρ^* can be obtained from the Manson–Coffin curve and the Smith–Watson–Topper (SWT) fatigue damage parameter [18]

$$D = \sigma_{\max} \frac{\Delta\varepsilon}{2} = \frac{(\sigma'_f)^2}{E}(2N)^{2b} + \sigma'_f \varepsilon'_f (2N)^{b+c}. \tag{1}$$

- The fatigue crack growth rate can be finally determined as:

$$\frac{\mathrm{d}a}{\mathrm{d}N} = \frac{\rho^*}{N}. \tag{2}$$

The mathematical formulation and computational procedure can be outlined as follows:

(1) For applied positive stress ratios ($R_{\mathrm{appl}} \geqslant 0$), the average elastic stresses over the first elementary material can be calculated by using the Creager–Paris solution [19] for a crack with the tip radius ρ^*

$$\tilde{\sigma}^e_{\max,\mathrm{net}} = \frac{\psi_{y,1} K_{\max,\mathrm{appl}}}{\sqrt{2\pi\rho^*}} = \frac{\psi_{y,1} S_{\max,\mathrm{appl}} Y \sqrt{\pi a}}{\sqrt{2\pi\rho^*}}$$
$$= S_{\max,\mathrm{appl}} Y \sqrt{\frac{a}{2\rho^*}} \psi_{y,1}, \tag{3}$$

$$\tilde{\sigma}^e_{\min,\mathrm{net}} = \frac{\psi_{y,1} K_{\min,\mathrm{appl}}}{\sqrt{2\pi\rho^*}} = \frac{\psi_{y,1} S_{\min,\mathrm{appl}} Y \sqrt{\pi a}}{\sqrt{2\pi\rho^*}}$$
$$= S_{\min,\mathrm{appl}} Y \sqrt{\frac{a}{2\rho^*}} \psi_{y,1}, \tag{4}$$

$$\Delta\tilde{\sigma}^e_{\mathrm{net}} = \frac{\psi_{y,1} K_{\max,\mathrm{appl}}}{\sqrt{2\pi\rho^*}} - \frac{\psi_{y,1} K_{\min,\mathrm{appl}}}{\sqrt{2\pi\rho^*}} = \frac{\psi_{y,1}}{\sqrt{2\pi\rho^*}} \Delta K_{\mathrm{appl}}$$
$$= \Delta S_{\mathrm{appl}} Y \sqrt{\frac{a}{2\rho^*}} \psi_{y,1}, \tag{5}$$

where $S_{\min,\mathrm{appl}} = \dfrac{K_{\min,\mathrm{appl}}}{Y\sqrt{\pi a}}$, $S_{\max,\mathrm{appl}} = \dfrac{K_{\max,\mathrm{appl}}}{Y\sqrt{\pi a}}$, $\Delta S_{\mathrm{appl}} = \dfrac{\Delta K_{\mathrm{appl}}}{Y\sqrt{\pi a}}$, $\psi_{y,1} = 1.633$.

(2) For applied negative stress ratios ($R_{\mathrm{appl}} < 0$), the crack surfaces contact with each other and the load is transferred through the crack surfaces except the region just behind the crack tip where the crack may stay open. Therefore, the crack tip region under compressive loading can be modeled as an elliptical or circular hole, as shown in Fig. 3b and load level 2. As a result, the net stress intensity factor (SIF) experienced at the minimum load is not the same as it would be for a fully active crack. The circular hole model of the crack under compression (Fig. 3b and load level 2) results [11] in the following SIF.

$$K_{\min,\mathrm{net}} = K_{\min,\mathrm{appl}} \frac{3}{2Y} \sqrt{\frac{\rho^*}{a}}. \tag{6}$$

It can be concluded, based on the proposed model, that the compressive part of a loading cycle is not very effective as far as the FCG is concerned. Therefore, by using the net SIF, the net elastic stresses can be obtained from the following equations:
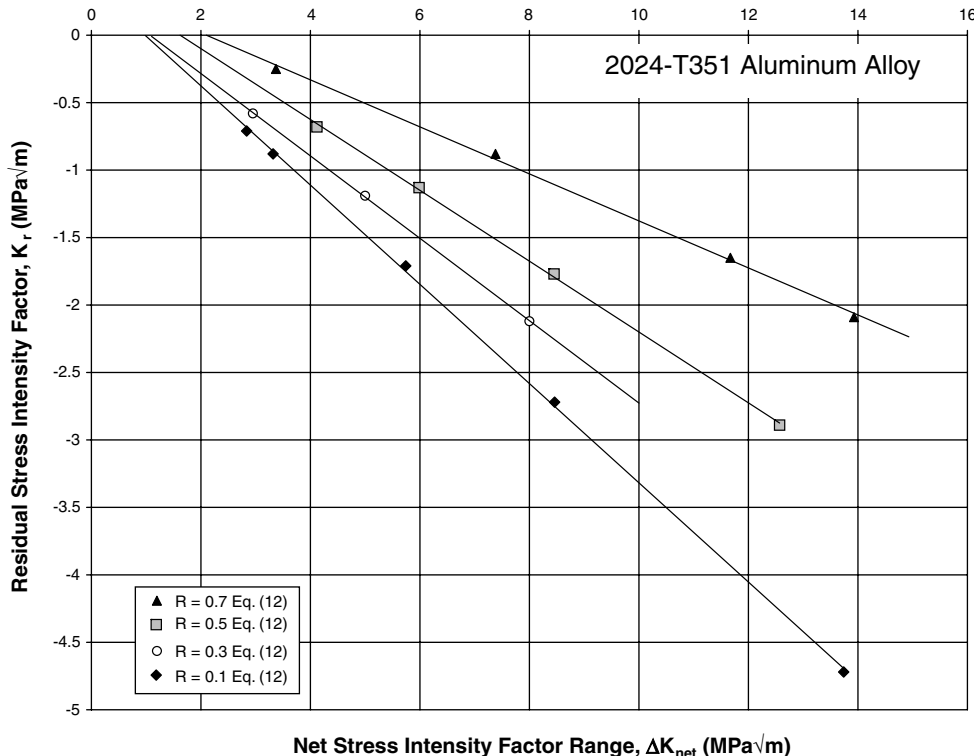

Fig. 4. Linear interpolation of the residual stress intensity factor for 2024-T351 aluminum alloy.

$$\tilde{\sigma}_{\text{max,net}}^{\text{e}} = \frac{\psi_{y,1} K_{\text{max,appl}}}{\sqrt{2\pi\rho^*}} = \frac{\psi_{y,1} S_{\text{max,appl}} Y \sqrt{\pi a}}{\sqrt{2\pi\rho^*}}$$

$$= S_{\text{max,appl}} Y \sqrt{\frac{a}{2\rho^*}} \psi_{y,1}, \tag{7}$$

$$\sigma_{\text{min,net}}^{\text{e}} = \frac{\psi_{y,1} K_{\text{min,net}}}{\sqrt{2\pi\rho^*}} = \frac{3\psi_{y,1}}{2\sqrt{2}} \frac{K_{\text{min,appl}}}{Y\sqrt{\pi a}} = S_{\text{min,appl}} \frac{3\psi_{y,1}}{2\sqrt{2}}, \tag{8}$$

$$\Delta\tilde{\sigma}_{\text{net}}^{\text{e}} = \tilde{\sigma}_{\text{max,net}}^{\text{e}} - \tilde{\sigma}_{\text{min,net}}^{\text{e}}$$

$$= \frac{\psi_{y,1}}{\sqrt{2\pi\rho^*}} \left(K_{\text{max,appl}} - \frac{3}{2Y} \sqrt{\frac{\rho^*}{a}} K_{\text{min,appl}} \right). \tag{9}$$

(3) The actual elasto-plastic stresses and strains are determined by using the above derived net stresses and the Neuber rule [20] over each material block ahead of the crack tip. The stress state over the first elementary material block is uni-axial if the body is in plane stress state; however, for other elements ahead of the crack tip, the stress state is bi-axial. Therefore, the multi-axial Neuber rule [21] and the Hencky equations of the total deformation theory of plasticity [22] were used for calculating elasto-plastic stresses and strains over each elementary material block. For the first elementary material block, the uni-axial Neuber rule and the Ramberg–Osgood take the form of Eqs. (10) and (11), respectively, for loading and unloading reversals

$$\begin{cases} \dfrac{1}{E} \left(\dfrac{K_{\text{max,net}} \times \psi_{y,1}}{\sqrt{2\pi\rho^*}} \right)^2 = \dfrac{(\tilde{\sigma}_{\text{max}}^{\text{a}})^2}{E} + \tilde{\sigma}_{\text{max}}^{\text{a}} \left(\dfrac{\tilde{\sigma}_{\text{max}}^{\text{a}}}{K'} \right)^{\frac{1}{n'}}, \\[4mm] \tilde{\varepsilon}_{\text{max}}^{\text{a}} = \dfrac{\tilde{\sigma}_{\text{max}}^{\text{a}}}{E} + \left(\dfrac{\tilde{\sigma}_{\text{max}}^{\text{a}}}{K'} \right)^{\frac{1}{n'}}, \end{cases} \tag{10}$$

$$\begin{cases} \dfrac{1}{E} \left(\dfrac{\Delta K_{\text{net}} \times \psi_{y,1}}{\sqrt{2\pi\rho^*}} \right)^2 = \dfrac{(\Delta\tilde{\sigma}^{\text{a}})^2}{E} + 2(\Delta\tilde{\sigma}^{\text{a}}) \left(\dfrac{\Delta\tilde{\sigma}^{\text{a}}}{2K'} \right)^{\frac{1}{n'}}, \\[4mm] \dfrac{\Delta\tilde{\varepsilon}^{\text{a}}}{2} = \dfrac{\Delta\tilde{\sigma}^{\text{a}}}{2E} + \left(\dfrac{\Delta\tilde{\sigma}^{\text{a}}}{2K'} \right)^{\frac{1}{n'}}. \end{cases} \tag{11}$$

The actual maximum stress and strain induced by the first reversal, and subsequent actual stress and strain ranges can be calculated from Eqs. (10) and (11), respectively.

(4) The residual stress field induced by the loading and unloading stress reversals was found by subtracting the stress range, $\Delta\tilde{\sigma}^{\text{a}}$, from the maximum stress, $\tilde{\sigma}_{\text{max}}^{\text{a}}$, at several locations ahead of the crack tip resulting in a distribution of the residual stress versus the distance from the crack tip. In order to simulate the character of the displacement field around the crack tip, the compressive part of the residual stress field ahead of the crack tip was symmetrically applied over the region behind the crack tip as shown in Fig. 2b.

(5) The residual stress effect can be quantified in terms of the residual stress intensity factor, K_{r}, which can be determined by using the weight function [23] method
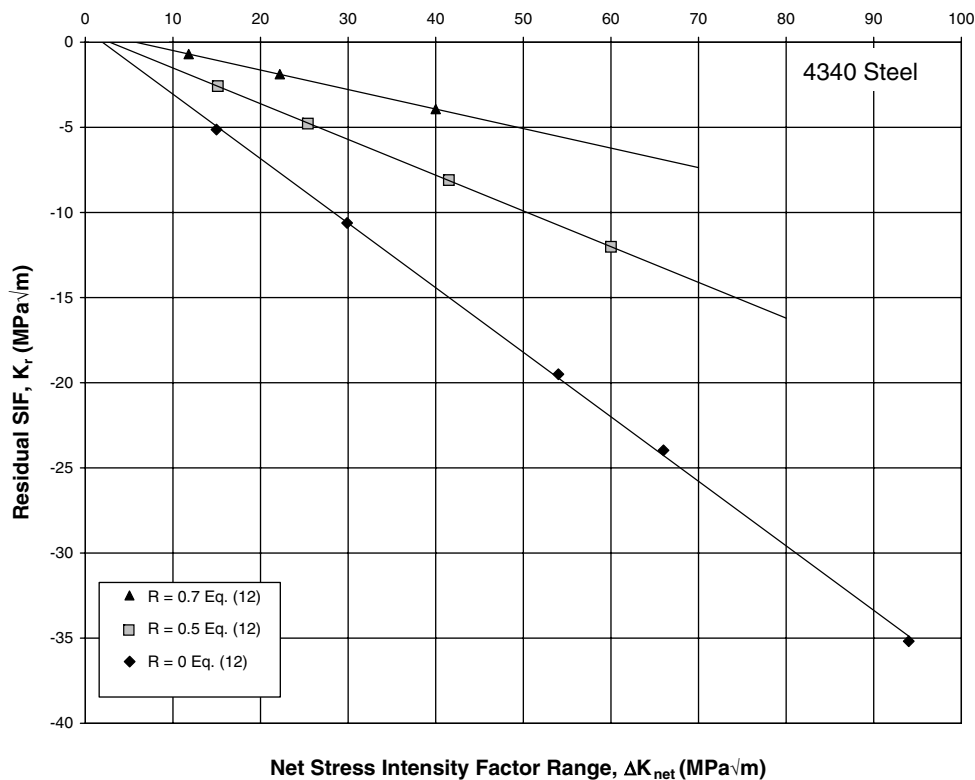

Fig. 5. Linear interpolation of the residual stress intensity factor for 4340 steel.

$$K_r = \int_0^a \sigma_r(x) m(x, a)\, dx, \tag{12}$$

where $\sigma_r(x)$ is the residual stress distribution shown in Fig. 2b and $m(x, a)$ is the universal weight function [24]

$$m(x, a) = \frac{2P}{\sqrt{2\pi(a - x)}}\left[1 + M_1\left(1 - \frac{x}{a}\right)^{\frac{1}{2}} + M_2\left(1 - \frac{x}{a}\right)^1 \right.$$
$$\left. + M_3\left(1 - \frac{x}{a}\right)^{\frac{3}{2}}\right]. \tag{13}$$

The factors M_1, M_2 and M_3 are dependent on the specimen geometry and are given in Refs. [25,26].

The residual stress intensity factor can be calculated from Eq. (12) for any stress ratio and any load magnitude. It was found that when the calculated residual stress intensity factors for any constant stress ratio are plotted against the net stress intensity range, a linear relationship of the K_r versus ΔK_{net} can be obtained. The linear $K_r - \Delta K_{net}$ relationships for the Al 2024-T351 and St-4340 materials are shown in Figs. 4 and 5, respectively. Moreover, the slope of the K_r versus ΔK_{net} line decreases with the increasing stress ratio, R. Knowing the linear relationship of the K_r versus ΔK_{net}, the residual stress intensity factor, K_r, can be obtained for any load magnitude without using Eq. (12). Application of the linear relation between the residual stress intensity factor and the net stress intensity range can significantly decrease the computational time required for the fatigue crack growth analysis.

3. Total stress intensity factors, $K_{max,tot}$ and ΔK_{tot}

After calculating the residual stress intensity factor, K_r, it is necessary to modify the applied $K_{max,appl}$ and ΔK_{appl} in order to account for the effect of the residual stress on the fatigue crack growth. The interactions of the stress intensity factor, the plastic zone and the residual stress manifest themselves through the change (decrease) of the resultant maximum stress intensity factor, $K_{max,tot}$, without significant changes in the resultant minimum stress intensity factor, $K_{min,tot}$ (Fig. 1a). It is assumed that the residual stress intensity factor, K_r, contributes mainly to the change (decrease) of the resultant maximum stress intensity factor, $K_{max,tot}$, and subsequently to the resultant stress intensity range, ΔK_{tot}. However, the magnitude of the residual stress effect depends on the applied stress ratio and it has to be treated differently for positive and negative applied stress ratios, R_{appl}.

3.1. Calculation of total stress intensity factors at positive stress ratios, $R_{appl} \geqslant 0$

The reversed plastic deformations around the crack tip induced at relatively high stress ratios ($R_{appl} > 0.5$) and relatively small stress intensity ranges (near threshold FCG), are usually not sufficient to produce compressive residual stresses. Therefore, the residual stress intensity factor is

close to zero ($K_r = 0$) and the total SIFs are the same as the applied ones:

$$K_{max,tot} = K_{max,net} = K_{max,appl}, \tag{14}$$
$$K_{min,tot} = K_{min,net} = K_{min,appl}, \tag{15}$$
$$\Delta K_{tot} = \Delta K_{net} = \Delta K_{appl}. \tag{16}$$

However, either for other positive stress ratios ($0 \leqslant R_{appl} \leqslant 0.5$) or for relatively high stress ratios ($R_{appl} > 0.5$) and high stress intensity ranges (medium range FCG rates), the residual stresses at the crack tip can change the effectiveness of applied SIFs. The maximum total stress intensity factor, $K_{max,tot}$, is calculated in such a case by adding the negative residual stress intensity factor, K_r, to the maximum applied stress intensity factor, $K_{max,appl}$. However, the minimum total SIF is assumed to be unaffected by the residual stress and equals the applied minimum SIF, $K_{min,appl}$. In such a case, the total SIFs are calculated as:

$$K_{max,tot} = K_{max,net} + K_r = K_{max,appl} + K_r, \tag{17}$$
$$K_{min,tot} = K_{min,net} = K_{min,appl}, \tag{18}$$
$$\Delta K_{tot} = \Delta K_{appl} + K_r. \tag{19}$$

3.2. Calculation of total stress intensity factors at negative stress ratios, $R_{appl} < 0$

In the case of negative stress ratios $R_{appl} < 0$, the maximum total (resultant) stress intensity factor, $K_{max,tot}$, is calculated analogously as in the case of $R_{appl} \geqslant 0$, i.e. the $K_{max,tot}$ is the algebraic sum of the maximum net, $K_{max,net}$, and the negative K_r residual stress intensity factor. However, the compressive part of the loading cycle is not entirely effective as far as FCG is concerned. Therefore, the minimum net stress intensity factor $K_{min,net}$, is not equal to the applied one and needs to be determined according to Eq. (6). Thus, all the stress intensity quantities at negative stress ratios can be determined from the following equations:

$$K_{max,tot} = K_{max,net} + K_r = K_{max,appl} + K_r, \tag{20}$$
$$K_{min,tot} = K_{min,net} = K_{min,appl}\frac{3}{2Y}\sqrt{\frac{\rho^*}{a}}, \tag{21}$$
$$\Delta K_{tot} = K_{max,tot} - K_{min,tot}$$
$$= K_{max,appl} + K_r - K_{min,appl}\frac{3}{2Y}\sqrt{\frac{\rho^*}{a}}$$
$$= \Delta K_{net} + K_r. \tag{22}$$

The resultant (total) SIF range, ΔK_{tot}, and the resultant (total) maximum SIF, $K_{max,tot}$, are the two main parameters used for fatigue crack growth predictions. However, they need to be combined into one driving force similar to the fatigue damage parameter used in the classical fatigue theories.

4. Analytical derivation of the unified two-parameter fatigue crack driving force $\Delta\kappa$ and the fatigue crack growth expression $da/dN - \Delta\kappa$

Noroozi et al. [11] derived the FCG equation in terms of a unified two-parameter driving force assuming predominately plastic material deformation at the crack tip while modeling the high fatigue crack growth rate, and the elastic behavior for the near threshold fatigue crack growth. Fatigue crack growth expressions derived for the two different material behaviors [11] are given below.

4.1. Predominantly plastic material behavior at the crack tip

$$\frac{da}{dN} = C\left[(K_{max,tot})^p(\Delta K_{tot})^{1-p}\right]^\gamma, \tag{23}$$

where

$$C = 2\rho^*\left[\frac{(\psi_{y,1})^2}{2^{\frac{n'+3}{n'+1}}\sigma'_f\varepsilon'_f\pi E\rho^*}\right]^{-\left(\frac{1}{b+c}\right)}; \quad p = \frac{n'}{n'+1}; \quad \gamma = -\frac{2}{b+c}.$$

4.2. Predominantly elastic material behavior at the crack tip

$$\frac{da}{dN} = C\left[(K_{max,tot})^p(\Delta K_{tot})^{1-p}\right]^\gamma, \tag{24}$$

where

$$C = 2\rho^*\left[\frac{(\psi_{y,1})^2}{4\pi\rho^*\sigma'^2_f}\right]^{-\frac{1}{2b}}; \quad p = 0.5; \quad \gamma = -\frac{1}{b}.$$

However, it is often observed in practice that in notched machine components subjected to service cyclic loading the maximum notch tip strains are predominantly plastic but the subsequent strain ranges are predominantly elastic. Therefore, analogous expressions as those above were derived assuming the mixed elasto-plastic behavior of the crack tip material subjected to cyclic loading.

4.3. Elasto-plastic material behavior at the crack tip

The average stress over the first crack tip material volume ρ^* induced by the applied stress intensity factor, was determined as previously using the Neuber rule, and the Ramberg–Osgood material stress–strain curve

$$\begin{cases} \frac{1}{E}\left(\frac{K_{max,tot} \times \psi_{y,1}}{\sqrt{2\pi\rho^*}}\right)^2 = \frac{(\tilde{\sigma}^a_{max})^2}{E} + \tilde{\sigma}^a_{max}\left(\frac{\tilde{\sigma}^a_{max}}{K'}\right)^{\frac{1}{n'}}, \\ \tilde{\varepsilon}^a_{max} = \frac{\tilde{\sigma}^a_{max}}{E} + \left(\frac{\tilde{\sigma}^a_{max}}{K'}\right)^{\frac{1}{n'}}, \end{cases} \tag{25}$$

$$\begin{cases} \frac{1}{E}\left(\frac{\Delta K_{tot} \times \psi_{y,1}}{\sqrt{2\pi\rho^*}}\right)^2 = \frac{(\Delta\tilde{\sigma}^a)^2}{E} + 2(\Delta\tilde{\sigma}^a)\left(\frac{\Delta\tilde{\sigma}^a}{2K'}\right)^{\frac{1}{n'}}, \\ \frac{\Delta\tilde{\varepsilon}^a}{2} = \frac{\Delta\tilde{\sigma}^a}{2E} + \left(\frac{\Delta\tilde{\sigma}^a}{2K'}\right)^{\frac{1}{n'}}. \end{cases} \tag{26}$$

It was assumed that the crack tip strains induced by the maximum load were predominantly plastic, while the strain ranges were predominantly elastic. Therefore, Eqs. (25) and (26) take the following forms:

$$\begin{cases} \frac{1}{E}\left(\frac{K_{max,tot} \times \psi_{y,1}}{\sqrt{2\pi\rho^*}}\right)^2 = \sigma^a_{max}\left(\frac{\tilde{\sigma}^a_{max}}{K'}\right)^{\frac{1}{n'}}, \\ \tilde{\varepsilon}^a_{max} = \left(\frac{\tilde{\sigma}^a_{max}}{K'}\right)^{\frac{1}{n'}}, \end{cases} \tag{27}$$

$$\begin{cases} \frac{1}{E}\left(\frac{\Delta K_{tot} \times \psi_{y,1}}{\sqrt{2\pi\rho^*}}\right)^2 = \frac{(\Delta\tilde{\sigma}^a)^2}{E}, \\ \frac{\Delta\tilde{\varepsilon}^a}{2} = \frac{\Delta\tilde{\sigma}^a}{2E}. \end{cases} \tag{28}$$

The plastic term in the Manson-Coffin (SWT) equation (1) was also omitted

$$\tilde{\sigma}^a_{max}\frac{\Delta\tilde{\varepsilon}^a}{2} = \frac{(\sigma'_f)^2}{E}(2N)^{2b}. \tag{29}$$

Using Eqs. (2) and (27)–(29), the final FCG expression was derived in the form of the following equation:

$$\frac{da}{dN} = C\left[(K_{max,tot})^p(\Delta K_{tot})^{0.5}\right]^\gamma, \tag{30}$$

where

$$C = 2\rho^*\left[\frac{1}{2(\sigma'_f)^2} \times \left[\left(\frac{\psi_{y,1}}{\sqrt{2\pi\rho^*}}\right)^{3n'+1} \times \frac{K'}{E^{n'}}\right]^{\frac{1}{n'+1}}\right]^{\frac{-1}{2b}};$$

$$p = \frac{n'}{n'+1}; \quad \gamma = -\frac{1}{b}.$$

The three sets of expressions (Eqs. (23), (24), and (30)) derived above indicate how the two SIF parameters, ΔK_{tot} and $K_{max,tot}$, characterizing the loading cycle should be combined into one driving force. It appears that the fatigue crack growth driving force should be of the form:

$$\Delta\kappa = K^p_{max,tot}\Delta K^{(1-p)}_{tot}. \tag{31}$$

It should also be noted that the derived driving force directly results from the mean stress correction model used in the analysis, i.e. the SWT fatigue damage parameter. All constants in the FCG equations above can be calculated based on the material properties given in the form of the Ramberg–Osgood stress–strain curve and the Manson–Coffin fatigue strain–life expression. The elementary material block size, ρ^*, must be determined separately.

5. Estimation of the elementary material block size, ρ^*

In order to determine the elementary material block size, ρ^*, some fatigue crack growth data are necessary. The obvious material properties are the threshold stress intensity factor ΔK_{th} and the fatigue limit $\Delta\sigma_{th}$. For the fatigue crack not to grow at the threshold stress intensity range, ΔK_{th}, the local stress at the crack tip must be equal to the fatigue limit, $\Delta\sigma_{th}$. Due to the fact that the fatigue limit is less than

the material yield limit, the elastic stress–strain analysis can be carried out. Thus, according to the Creager–Paris solution, the two material properties can be related using:

$$\Delta\tilde{\sigma}_{th}^{a} = \frac{\Delta K_{th} \times \psi_{y,1}}{\sqrt{2\pi\rho^*}}. \tag{32}$$

Eq. (33) may subsequently be used for the determination of the elementary material block size, ρ^*

$$\rho^* = \frac{(\psi_{y,1})^2}{2\pi}\left(\frac{\Delta K_{th}}{\Delta\tilde{\sigma}_{th}^{a}}\right)^2. \tag{33}$$

The elementary material block size equation (33) is in such a case close to the well-known parameter resulting from the Kitagawa diagram [27]. However, care must be taken in order to make sure that the fatigue limit $\Delta\tilde{\sigma}_{th}^{a}$ was obtained at the same stress ratio R as the stress ratio at the crack tip induced by the threshold stress intensity range ΔK_{th}. Further, some care needs to be taken while determining the threshold stress intensity factors. Namely, the fatigue crack may not grow due to one of the followings [10]: the applied maximum stress intensity factor is less than the maximum threshold stress intensity factor ($K_{max,appl} < K_{max,th}$), or the applied stress intensity range is less than the threshold stress intensity range ($\Delta K_{appl} < \Delta K_{th}$). If the crack ceases to grow at the stress ratio $R = 0$ it is not certain whether the maximum stress intensity or the stress intensity range has reached the threshold level. Therefore, the optimum stress ratio at which the threshold stress range ΔK_{th} can be determined, without producing significant plasticity at maximum stress intensity factor, is $0.2 < R < 0.3$ and in such a case the "elastic" solution, Eq. (33), can be used.

Because of the difficulties discussed above, when using Eq. (33), the estimation of the crack tip radius, ρ^*, can be carried out by using the experimental fatigue crack growth data and solving simultaneously the complete set of Eqs. (25), (26), and (34) which is obtained by substituting Eq. (2) into the Manson-Coffin together with the SWT parameter Eq. (1)

$$\tilde{\sigma}_{max}^{a}\frac{\Delta\tilde{\varepsilon}^{a}}{2} = \frac{(\sigma_f')^2}{E}\left(\frac{2\rho^*}{da/dN}\right)^{2b} + \sigma_f'\varepsilon_f'\left(\frac{2\rho^*}{da/dN}\right)^{b+c}. \tag{34}$$

Depending on the nature of available experimental fatigue crack growth data, different methods for estimating the ρ^* parameter can be suggested.

If the near threshold fatigue crack growth data at high stress ratios $R_{appl} > 0.5$ is available, the estimation of the crack tip radius, ρ^*, can be found by using the applied stress intensity factors. At high stress ratios and close to the threshold, the total stress intensity factors, $K_{max,tot}$ and ΔK_{tot}, have the same magnitudes as the applied ones. Therefore, the applied SIFs can be used in Eqs. (25) and (26) consequently the ρ^* parameter can be estimated from Eqs. (25), (26), and (34) by using the iteration technique. Due to scatter of fatigue crack growth data, it is recommended that several near threshold FCG data points are selected. The ρ^* parameter can then be calculated for each FCG data point. The average of the calculated ρ^* parameters is considered as the ρ^* parameter for a particular material.

In order to determine the elementary material block size ρ^* in the absence of the near threshold fatigue crack growth data, one set of fatigue crack growth data obtained at any stress ratio is sufficient. The ρ^* parameter can be obtained by using the iteration technique. First, the residual SIF, K_r, can be determined for the assumed ρ^* magnitude followed by the determination of the total stress intensity factors, $K_{max,tot}$ and ΔK_{tot}, corresponding to given experimental FCG reference data points. The total stress intensity factors are used to calculate the magnitude of the two-parameter driving force, $\Delta\kappa = K_{max,tot}^{p}\Delta K_{tot}^{(1-p)}$. Second, the experimental fatigue crack growth data points can be plotted in terms of the two-parameter driving force, da/dN versus $K_{max,tot}^{p}\Delta K_{tot}^{(1-p)}$. Finally, using Eqs. (25), (26), (34) and the assumed ρ^* parameter, the numerically derived FCG curve (exact solution) can be drawn (Fig. 6) in the same system of coordinates, da/dN versus $K_{max,tot}^{p}\Delta K_{tot}^{(1-p)}$. If the numerically derived FCG curve is in a good agreement
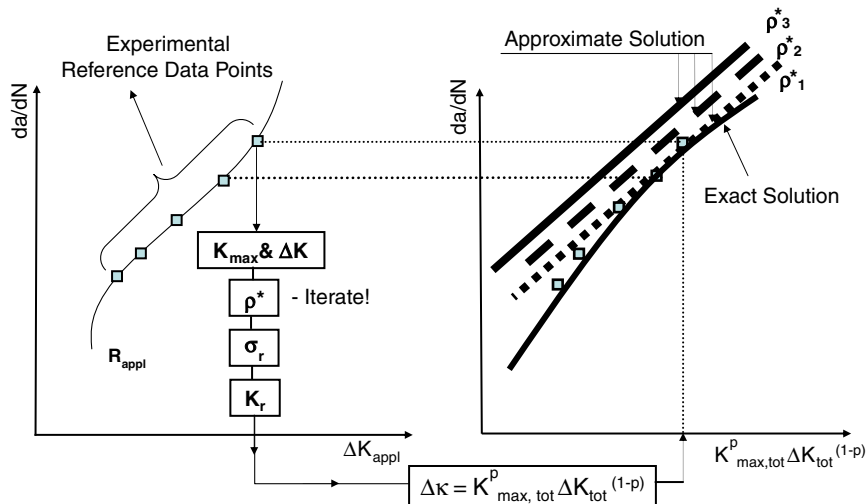

Fig. 6. Schematic iterative determination of ρ^* parameter using high FCG data at any R-ratio.

Table 1
Material properties and the elementary material block size (crack tip radius) ρ^*

Material	Al 2024-T351	St-4340	Ti–6Al–4V
Monotonic material properties			
E (MPa)	70,000	200,000	117,000
v	0.32	0.3	0.3
σ_{ys} (MPa)	403.46	889.32	1185
Cyclic stress–strain			
K' (MPa)	751.5	1910	1772
n'	0.1	0.123	0.106
Strain–life curve			
σ_f' (MPa)	909.48	1879	2030
b	−0.1	−0.0859	−0.104
ε_f'	0.36	0.64	0.841
c	−0.65	−0.636	−0.688
Crack tip radius			
ρ^* (m)	8×10^{-6}	2×10^{-6}	8×10^{-6}

with the experimental FCG data points, the initial assumption for the magnitude of the ρ^* parameter was correct. Otherwise, the entire process needs to be iterated until the correct ρ^* is determined. In this method, the estimation of the ρ^* parameter needs several iterations which are time consuming. Therefore, instead of using the exact solution, the approximate solution resulting from Eq. (23) can be used for the comparison with the experimental FCG reference data points. However, it is recommended to use the

high-rate fatigue crack growth data as the reference because the high-rate FCG is governed predominantly by plastic strains and the use of Eq. (23) is justified. Moreover, at high fatigue crack growth rates, the approximate solution is almost the same as the exact solution.

6. Verification of the proposed model

Three forms of the fatigue crack driving force, $K_{max,tot}^p \Delta K_{tot}^{(1-p)}$, $K_{max,tot}^{0.5} \Delta K_{tot}^{0.5}$ and $K_{max,tot}^p \Delta K_{tot}^{0.5}$, have been derived from Eqs. (23), (24), and (30) for the plastic, elastic, and elasto-plastic material behavior at the crack tip, respectively. The two-parameter fatigue crack growth driving forces were used to model the effect of the stress ratio R on the fatigue crack growth under constant amplitude loading. The total stress intensity factors corrected for the residual stress effect were used to determine the magnitude of each driving force.

The "approximate" closed solutions, in the form of Eqs. (23), (24), and (30), were attainable after neglecting the plastic or elastic terms in the Ramberg–Osgood and the Manson–Coffin equations. Unfortunately, such solutions become inaccurate in the regions where both terms are equally important. However, numerical solutions to the complete set of Eqs. (25), (26), and (34), i.e. without neglecting any terms, are possible to obtain. The final solution cannot be derived in a closed form but it can be presented graphically. The numerical solution is termed further on as the "exact solution".
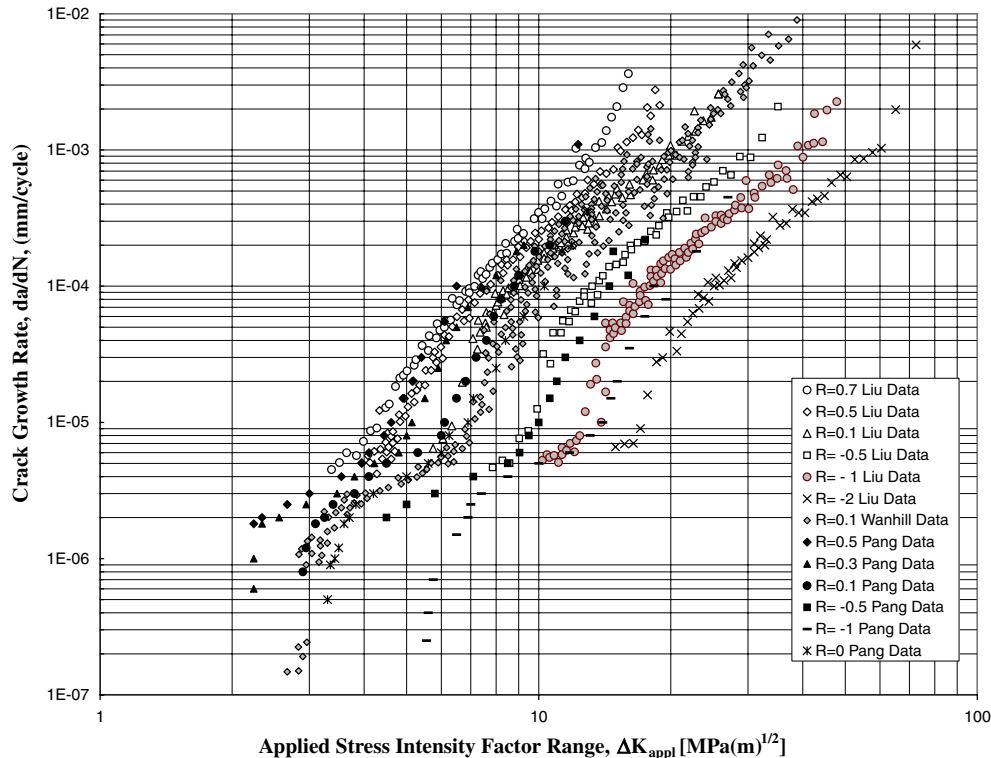

Fig. 7. Fatigue crack growth data for 2024-T351 aluminum alloy obtained at stress ratios $-2 \leqslant R \leqslant 0.7$ [28–30].

Table 2
Parameters and constants of the two-parameter fatigue crack growth model

Material	Al 2024-351	St-4340	Ti–6Al–4V
Plastic			
γ	2.67	2.77	2.53
p	0.09	0.11	0.096
C	9.13×10^{-10}	4.25×10^{-11}	1×10^{-10}
Elastic			
γ	10	11.64	9.62
p	0.5	0.5	0.5
C	5.43×10^{-13}	5.25×10^{-15}	4.67×10^{-16}
Elastic–plastic			
γ	10	11.64	9.62
p	0.09	0.11	0.096
C	8.72×10^{-12}	1.83×10^{-13}	1.88×10^{-13}

Fatigue crack growth data for three materials were used to show the stress ratio effect on fatigue crack growth, i.e., aluminum alloy A1 2024-T351, steel alloy St-4340, and titanium alloy Ti–6Al–4V. The cyclic and fatigue properties for all materials are given in Table 1.

6.1. Modeling of fatigue crack growth in the Al 2024-T351 alloy

The fatigue crack growth data for the Al 2024-T351 aluminum alloy was found in Refs. [28–30]. The fatigue crack growth data sets were obtained at various stress ratios,

R_{appl}, and are shown in Fig. 7 as a function of the applied stress intensity factor range, ΔK_{appl}.

The cyclic and fatigue properties for the Al 2024-T351 aluminum alloy were obtained from Ref. [31], as listed in Table 1, but the same data can also be found on the Society of Automotive Engineers (SAE) web site (fde.uwaterloo.ca) maintained by the Fatigue Design and Evaluation Committee. Due to the availability of the near threshold data obtained at high stress ratios, the ρ^* parameter was determined from Eqs. (25), (26), and (34), as described in Section 5, and is listed in Table 1. Based on the material data listed in Table 1 and the determined ρ^* parameter, the constants of Eqs. (23), (24), and (30) were calculated (Table 2). It is seen (Fig. 8) that in the high and medium FCG rate regimes, the "plastic" driving force, $K_{max,tot}^p \Delta K_{tot}^{(1-p)}$, was successful in correlating the fatigue crack growth data obtained at various stress ratios. The "elastic" driving force, $K_{max,tot}^{0.5} \Delta K_{tot}^{0.5}$, was the least successful one even in the near threshold region (Fig. 9). It can be noted that the elastic driving force may be used only to consolidate FCG data at very low fatigue crack growth rates; therefore, it should not be used for fatigue crack growth predictions away from the threshold. However, it was found (Fig. 10) that the combination of the elastic and plastic stress–strain material behavior at the crack tip in the form of the "mixed" driving force, $K_{max,tot}^p \Delta K_{tot}^{0.5}$, could be used to correlate FCG data at various R-ratios for the FCG rates spanning from the near threshold to the
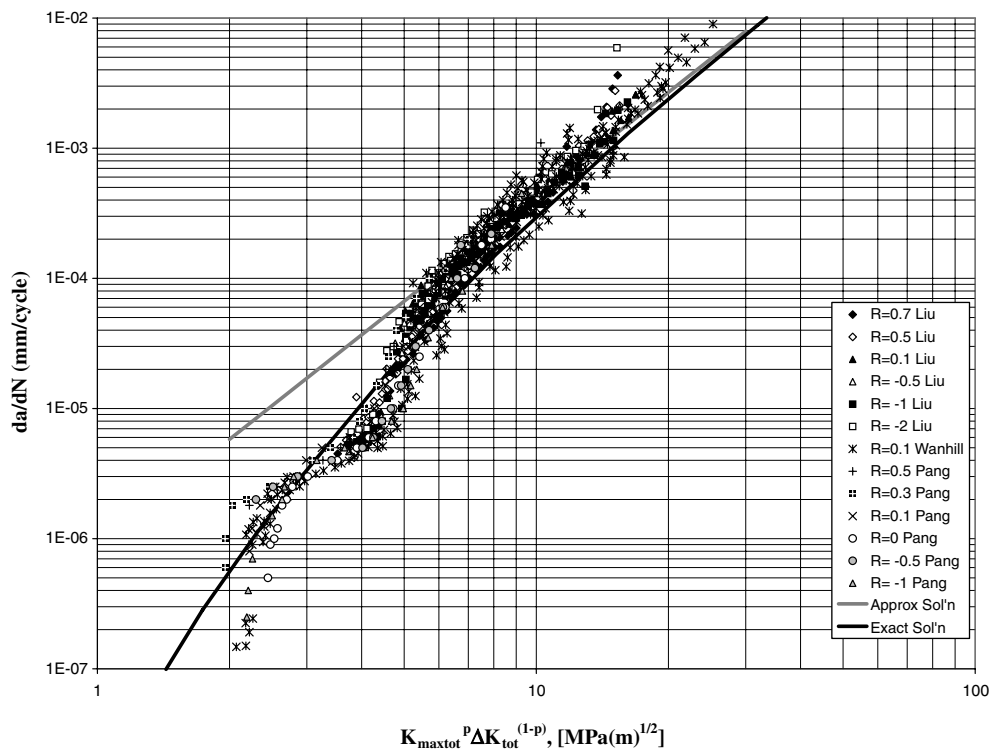

Fig. 8. Fatigue crack growth as a function of the "plastic" two-parameter driving force, $K_{max,tot}^p \Delta K_{tot}^{(1-p)}$, for 2024-T351 Al alloy.
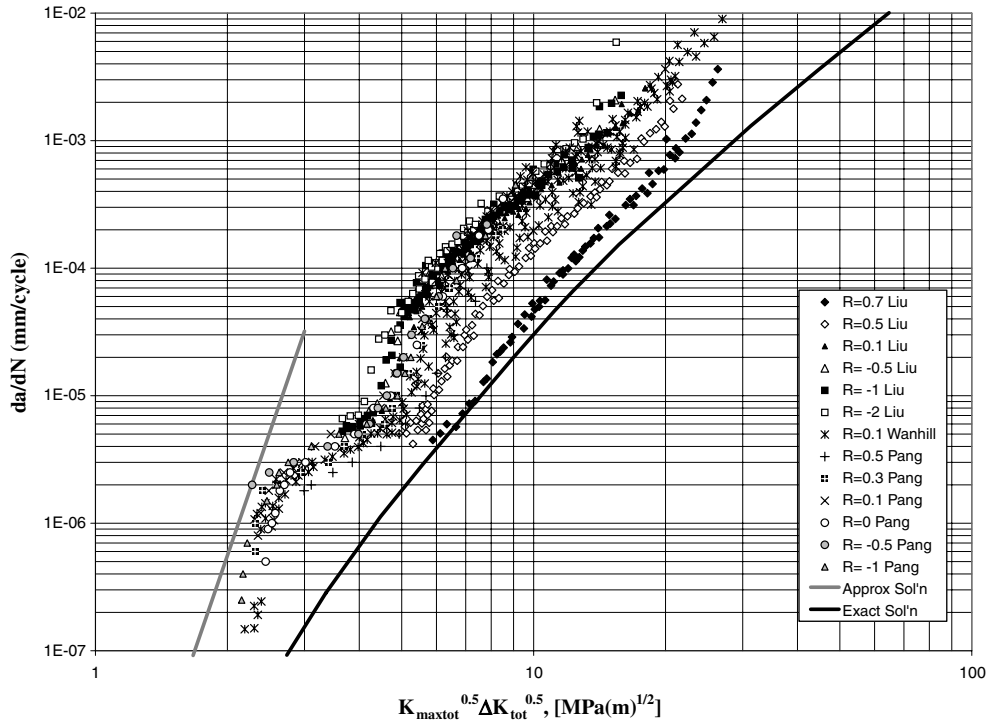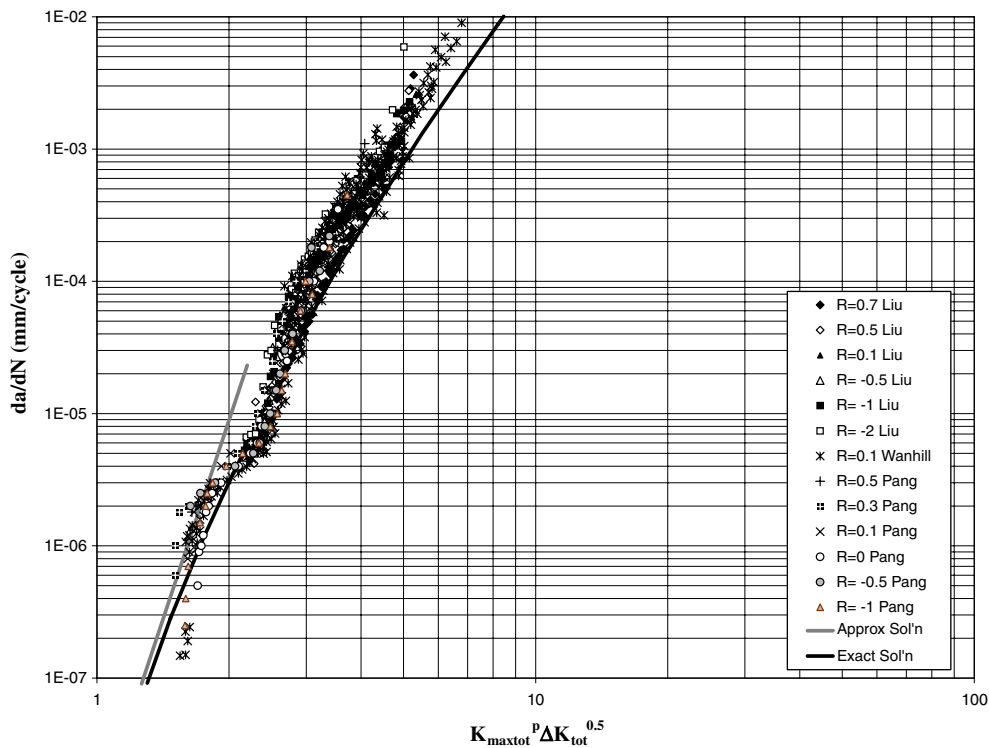
Fig. 9. Fatigue crack growth as a function of the "elastic" two-parameter driving force, $K_{\max,tot}^{0.5}\Delta K_{tot}^{0.5}$, for 2024-T351 Al alloy.

high growth rate regime. Both the "exact" FCG curves and the approximate closed form solutions (Eqs. (23), (24), and (30)) are shown as diagrams (Figs. 8–10) where the fatigue crack growth rate is shown as a function of the appropriate driving force $\Delta\kappa$. The best results in correlating the FCG under various stress ratios were obtained while using the mixed driving force in the form of $K_{\max,tot}^{p}\Delta K_{tot}^{0.5}$.

Fig. 10. Fatigue crack growth as a function of the "mixed" two-parameter driving force, $K_{\max,tot}^{p}\Delta K_{tot}^{0.5}$, for 2024-T351 Al alloy.

6.2. Modeling of fatigue crack growth in the 4340 steel material

The fatigue crack growth data for the 4340 steel alloy was found in Refs. [32–35]. The fatigue crack growth data sets were obtained at various stress ratios, R_{appl}, and are shown in Fig. 11 as a function of the applied stress intensity factor range, ΔK_{appl}.

The cyclic and fatigue properties for the 4340 steel alloy were obtained from Ref. [32] and are listed in Table 1. Due to the availability of the near threshold data obtained at high stress ratios, the ρ^* parameter was determined from Eqs. (25), (26), and (34), as described in Section 5, and is listed in Table 1. Based on the material data listed in Table 1 and the determined ρ^* parameter, the constants of Eqs. (23), (24), and (30) can be calculated and found in Table 2. It is seen (Fig. 12) that in the high and medium FCG rate regimes, the "plastic" driving force, $K_{max,tot}^{p}\Delta K_{tot}^{(1-p)}$, was successful in correlating the fatigue crack growth data obtained at various stress ratios. The "elastic" driving force, $K_{max,tot}^{0.5}\Delta K_{tot}^{0.5}$, was the least successful one even in the near threshold region (Fig. 13). It can be noted that the elastic driving force may be used only to consolidate FCG data at very low fatigue crack growth rates; therefore, similarly to the previous material it should not be used for fatigue crack growth predictions away from the threshold. It was also found (Fig. 14) that the combination of the elastic and plastic stress–strain material behavior at the crack tip in the form of the "mixed" driving force,

$K_{max,tot}^{p}\Delta K_{tot}^{0.5}$, could be used to correlate FCG data at various R-ratios for the FCG rates spanning from the near threshold to the high growth rate regime.

Both the "exact" FCG curves and the approximate closed form solutions (Eqs. (23), (24), and (30)) are shown as diagrams (Figs. 12–14) where the fatigue crack growth rates are plotted as a function of the appropriate driving force $\Delta\kappa$. The best results in correlating the FCG under various stress ratios were obtained while using the mixed driving force in the form of $K_{max,tot}^{p}\Delta K_{tot}^{0.5}$.

6.3. Modeling of fatigue crack growth in the Ti–6Al–4V material

The fatigue crack growth data for the Ti–6Al–4V alloy was found in Refs. [36,37]. The fatigue crack growth data sets were obtained at various stress ratios, R_{appl}, and are shown in Fig. 15 as a function of the applied stress intensity factor range, ΔK_{appl}.

The cyclic and fatigue properties for the Ti–6Al–4V alloy were obtained from Ref. [32] and are listed in Table 1. Due to the availability of the near threshold data obtained at high stress ratios, the ρ^* parameter was determined from Eqs. (25), (26), and (34), as described in Section 5, and is listed in Table 1. Based on the material data listed in Table 1 and the determined ρ^* parameter, the constants of Eqs. (23), (24), and (30) can be calculated and found in Table 2. It is seen (Fig. 16) that in the high and medium FCG rate regimes, the "plastic" driving force,
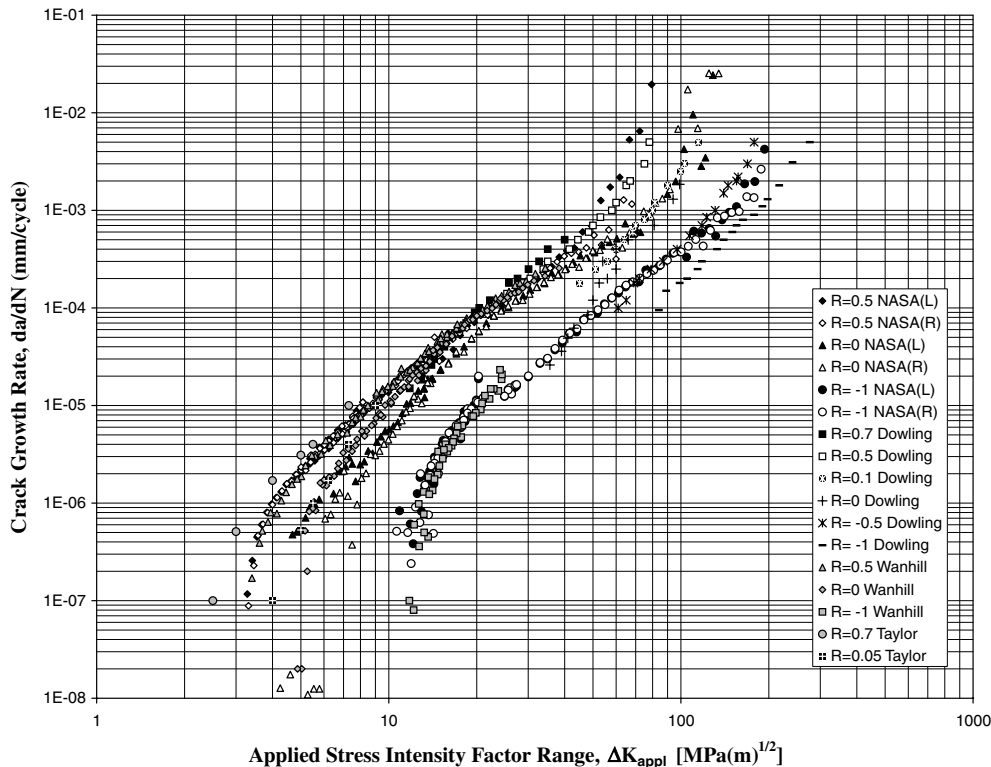

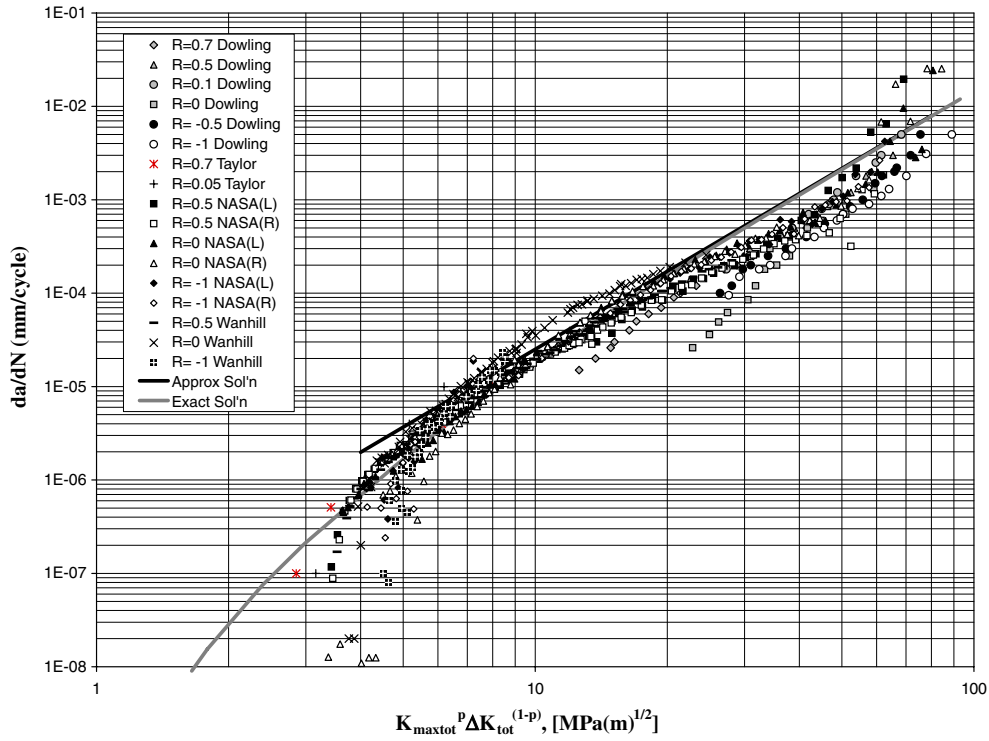Fig. 11. Fatigue crack growth data for 4340 steel obtained at stress ratios $-1 \leqslant R \leqslant 0.7$ [32–35].

Fig. 12. Fatigue crack growth as a function of the "plastic" two-parameter driving force, $K_{max,tot}^{p} \Delta K_{tot}^{(1-p)}$, for 4340 steel.
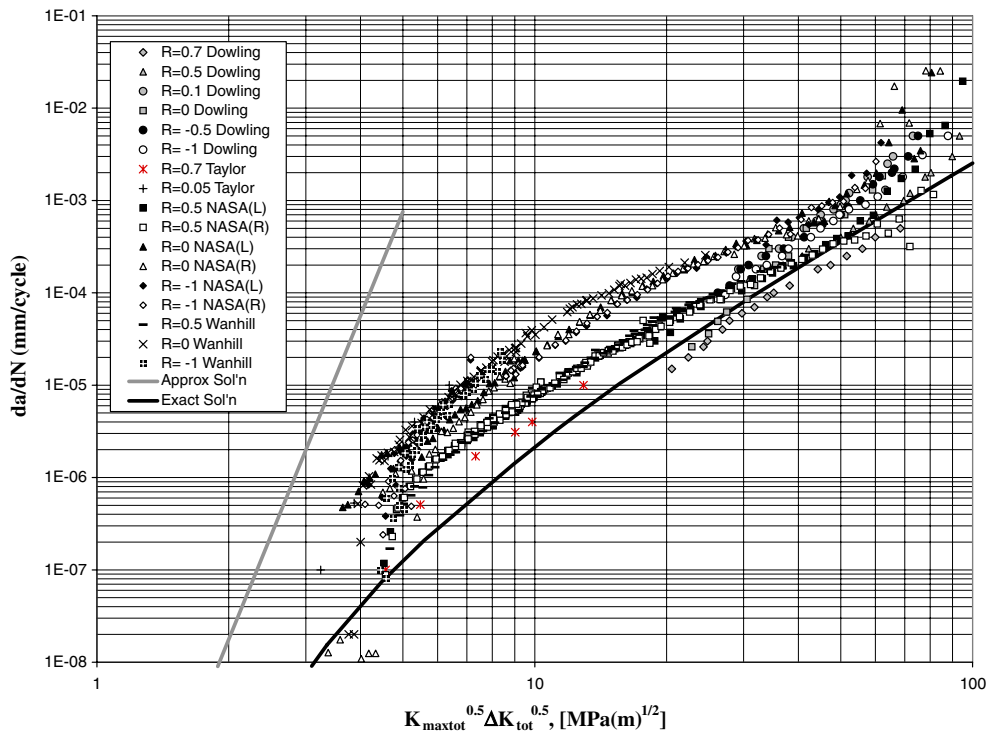

Fig. 13. Fatigue crack growth as a function of the "elastic" two-parameter driving force, $K_{max,tot}^{0.5} \Delta K_{tot}^{0.5}$, for 4340 steel.

$K_{max,tot}^{p} \Delta K_{tot}^{(1-p)}$, was successful in correlating the fatigue crack growth data obtained at various stress ratios. The "elastic" driving force, $K_{max,tot}^{0.5} \Delta K_{tot}^{0.5}$, was the least successful one even in the near threshold region (Fig. 17). It can be noted that the elastic driving force may be used only to consolidate FCG data at very low fatigue crack growth rates; therefore, it should not be used for fatigue crack growth predictions away from the threshold. However, it
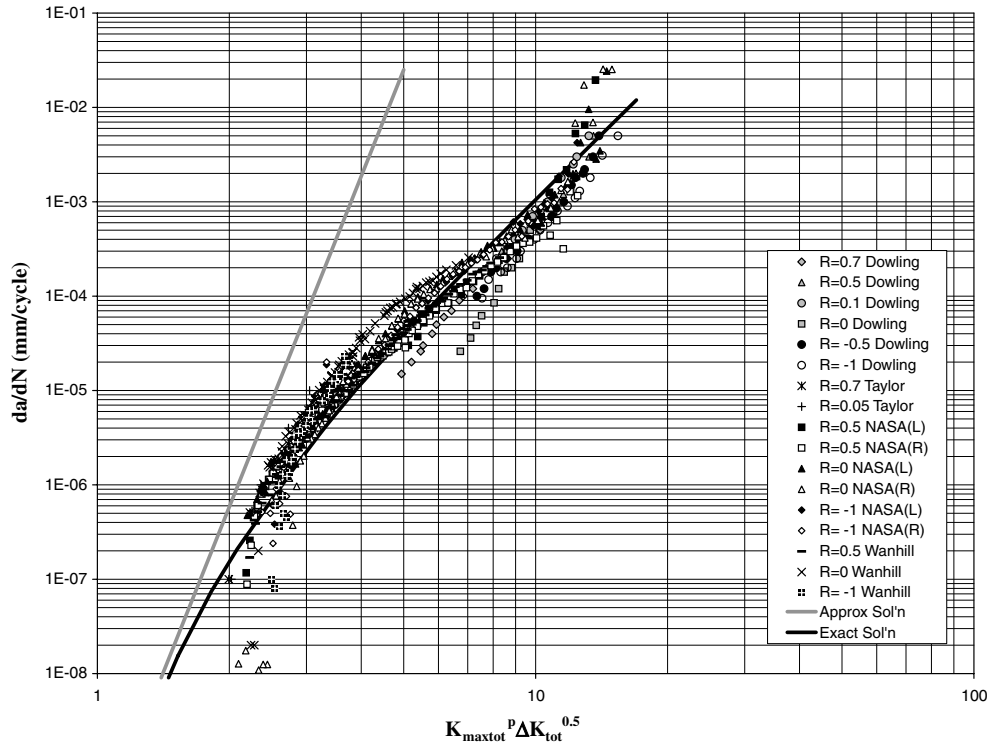
Fig. 14. Fatigue crack growth as a function of the "mixed" two-parameter driving force, $K_{max,tot}^p \Delta K_{tot}^{0.5}$, for 4340 steel.
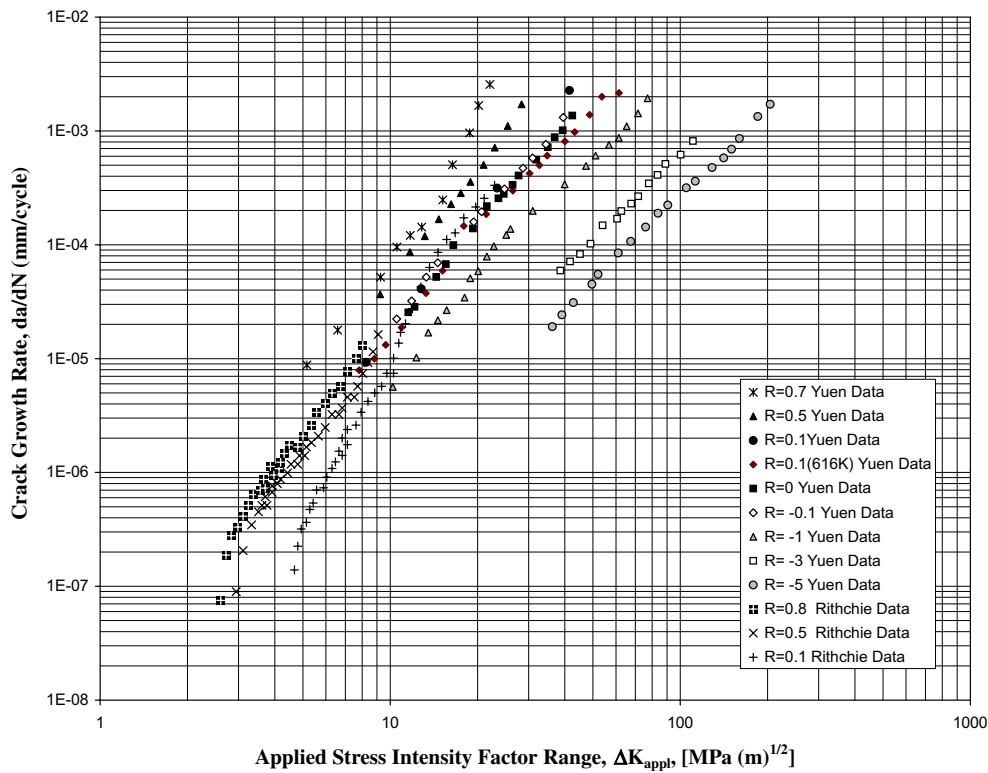

Fig. 15. Fatigue crack growth data for Ti–6Al–4V alloy obtained at stress ratios $-5 \leqslant R \leqslant 0.8$ [36,37].

was found (Fig. 18) that the combination of the elastic and plastic stress–strain material behavior at the crack tip in the form of the "mixed" driving force, $K_{max,tot}^p \Delta K_{tot}^{0.5}$, could be used to correlate FCG data at various R-ratios for the FCG rates spanning from the near threshold to the high growth rate regime.
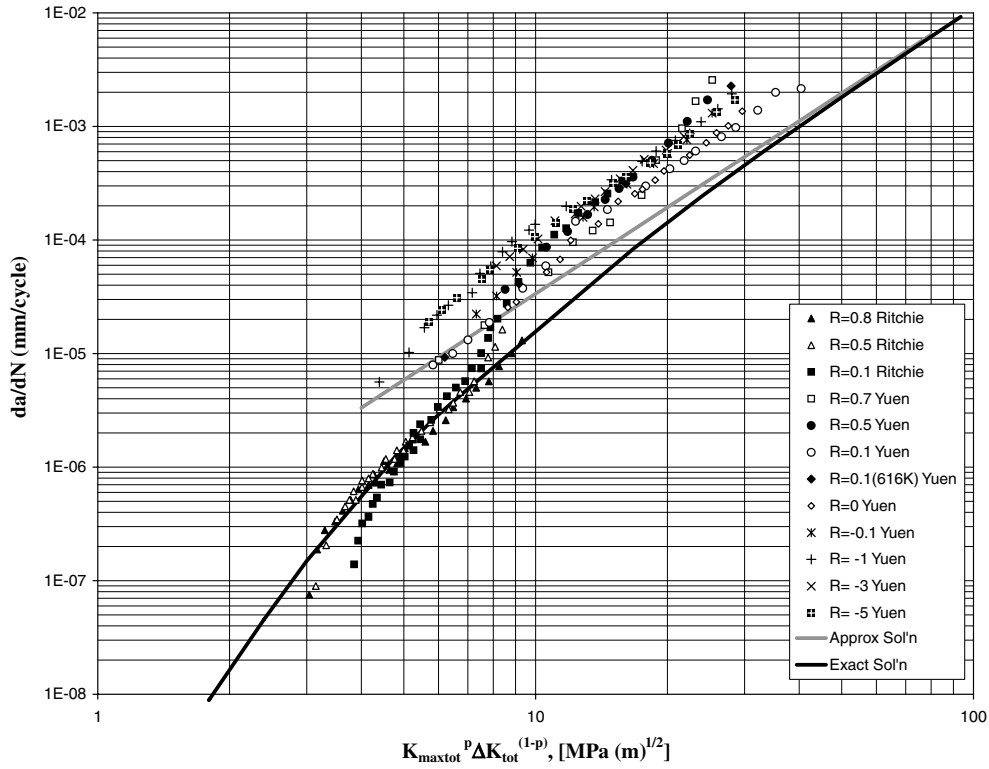
Fig. 16. Fatigue crack growth as a function of the "plastic" two-parameter driving force, $K^p_{\max,tot}\Delta K^{(1-p)}_{tot}$, for Ti–6Al–4V alloy.

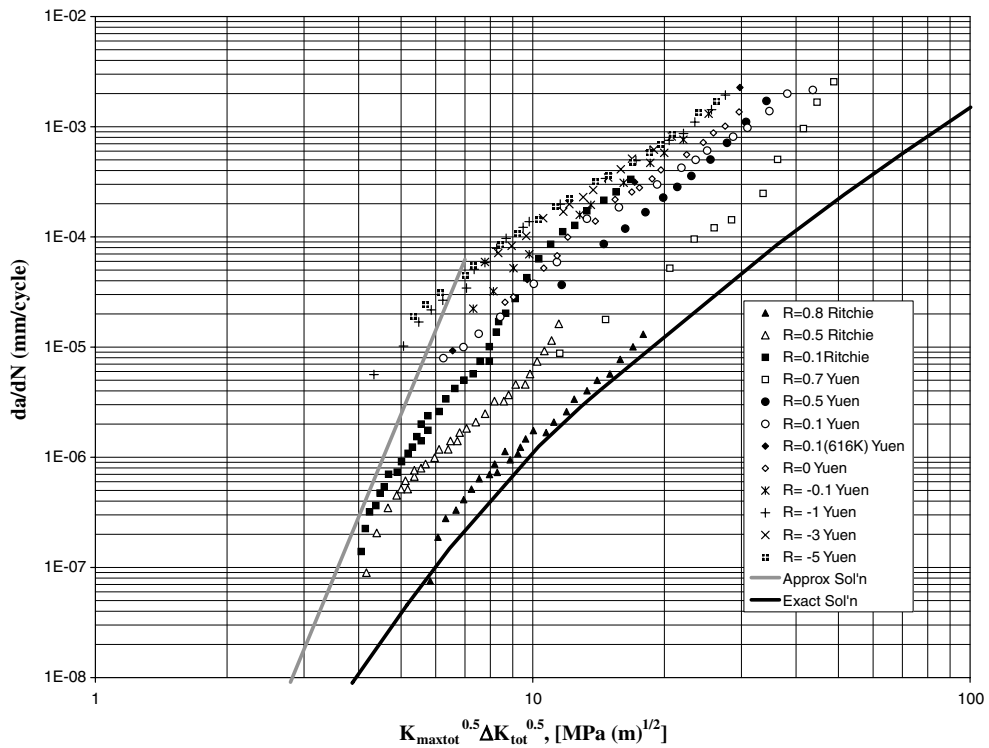Fig. 17. Fatigue crack growth as a function of the "elastic" two-parameter driving force, $K^{0.5}_{\max,tot}\Delta K^{0.5}_{tot}$, for Ti–6Al–4V alloy.

Both the "exact" FCG curves and the approximate closed form solutions (Eqs. (23), (24), and (30)) are shown as diagrams (Figs. 16–18) where the fatigue crack growth rate is plotted as a function of the appropriate driving force $\Delta\kappa$. The best results in correlating the FCG under various stress ratios were obtained while using the "mixed" driving
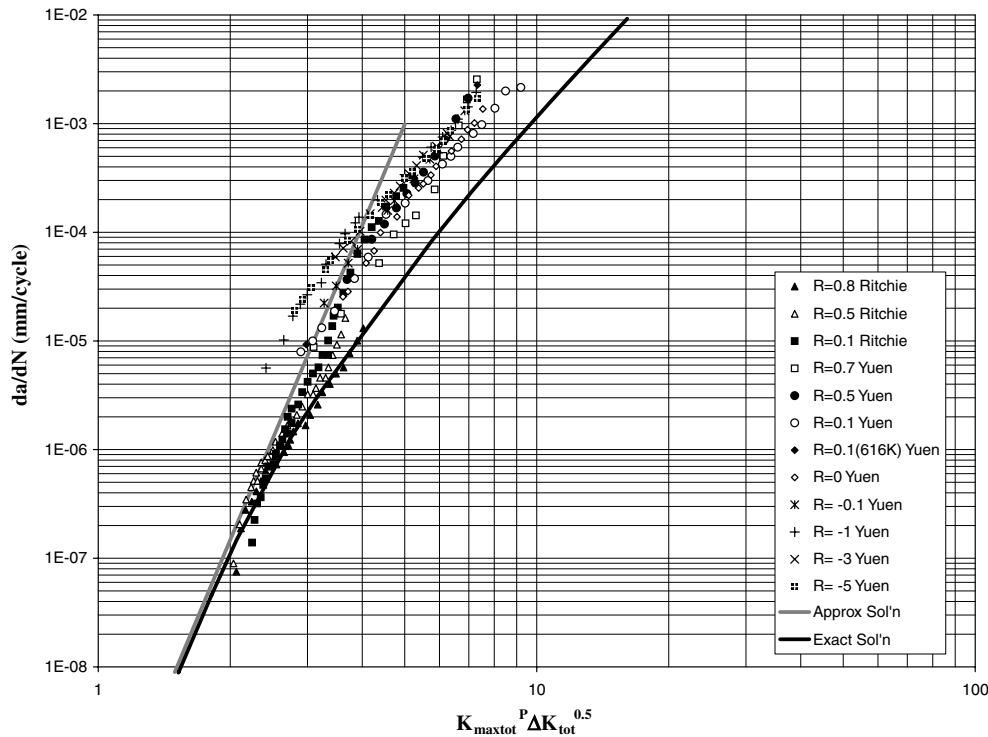
Fig. 18. Fatigue crack growth as a function of the "mixed" two-parameter driving force, $K_{\max,tot}^{p}\Delta K_{tot}^{0.5}$, for Ti–6Al–4V alloy.

force in the form of $K_{\max,tot}^{p}\Delta K_{tot}^{0.5}$. However, for fatigue crack growth rates more than 2×10^{-5} mm/cycle, there are some discrepancies between the predicted and experimental curves, as shown in Figs. 16 and 18. Although two different set of fatigue crack growth data were used for the comparisons, the "exact" FCG curves and the approximate closed form solutions were plotted using one set of cyclic and fatigue properties of the material. Probably, the Ti–6Al–4V specimen used to create the fatigue crack growth data, $da/dN > 2 \times 10^{-5}$ mm/cycle, has different cyclic and fatigue properties than the other one.

As shown in Fig. 10 (for 2024-T351 Al alloy), Fig. 14 (for 4340 steel) and Fig. 18 (for Ti–6Al–4V), the numerical exact solution presented in terms of the mixed driving force had a good agreement with the entire range of experimental FCG data. However, the elasto-plastic approximate solution agreed well with only the low FCG data. Therefore, it is recommended that in practice two lines da/dN vs. Δk should be fitted into the existing FCG data plotted in terms of the mixed driving force, i.e., one line covering the near threshold FCG data and the other approximating so called Paris' regime. The two power law curves characterized by two sets of constants (the exponent γ and the constant C) can be subsequently used for FCG analyses.

7. Conclusions

A fatigue crack growth model based on the simulation of the elastic–plastic stress–strain response at the crack tip has been proposed. The application of the model

resulted in the derivation of a two-parameter driving force combining the effect of the maximum stress intensity factor and the stress intensity range. It was shown that after correcting the applied stress intensity factors for the effect of the plasticity induced residual stresses near the crack tip, it was possible to derive one master fatigue crack growth curve valid for all stress ratios. The entire analysis was carried out as for classical notch without the necessity of introducing the concept of the crack closure behind the crack tip. It was also shown that the residual stress effect can be represented in terms of the residual stress intensity factor, K_r, which can subsequently be used to modify the applied intensity factors. The residual stress intensity factor changes linearly with respect to the net stress intensity factor range, ΔK_{net}, for any given stress ratio. It was also assumed that the residual stress effect can change only the maximum applied stress intensity factor, $K_{max,appl}$, without changing the minimum applied stress intensity factor, $K_{min,appl}$. This idea is contrary to the closure concept which is based on the observation of the crack tip closure phenomenon implicating that the maximum applied SIF remains constant while the resultant minimum applied SIF changes.

Three forms of the fatigue crack driving force, $K_{\max,tot}^{p}\Delta K_{tot}^{(1-p)}$, $K_{\max,tot}^{0.5}\Delta K_{tot}^{0.5}$ and $K_{\max,tot}^{p}\Delta K_{tot}^{0.5}$, were derived depending on the assumptions concerning the nature of the crack tip stress–strain field. It was shown that the driving force in the form of $K_{\max,tot}^{p}\Delta K_{tot}^{0.5}$ could correlate FCG data for a wide range of stress ratios and FCG rates. The driving force $K_{\max,tot}^{p}\Delta K_{tot}^{(1-p)}$ could only be used for

predicting the high FCG rates. However, the driving force of $K_{max,tot}^{0.5}\Delta K_{tot}^{0.5}$ was not good for FCG predictions, even in the near threshold region.

The model was also able to account for the detrimental effect of the compressive part of a loading cycle. It was found that the contribution of the compressive part of the stress reversal was relatively small and depended on the crack tip radius, ρ^*, and the actual crack size, a. It is possible that the modeling of the crack tip as a circular hole might be non-conservative, which requires further study.

Acknowledgment

References

[1] Paris PC, Erdogan F. A critical analysis of crack propagation laws. J Basic Eng 1963;D85:528–34.

[2] Elber W. The significance of fatigue crack closure. In: Damage tolerance in aircraft structure. ASTM STP 486. American Society for Testing and Materials; 1971. p. 230–42.

[3] Macha DE, Corby DM, Jones JW. On the variation of fatigue-crack-opening load with measurement location. Proc Soc Exp Stress Anal 1979;19(6):207–13.

[4] Shih TT, Wei RP. A study of crack closure in fatigue. Eng Fract Mech 1974;6:19–32.

[5] Kirby BR, Beevers CJ. Slow fatigue crack growth and threshold behavior in air and vacuum of commercial aluminum alloys. Fatigue Int Mater 1979;1:203–15.

[6] Kujawski D. A new $(\Delta K^+ K_{max})^{0.5}$ driving force parameter for crack growth in aluminum alloys. Int J Fatigue 2001;23:733–40.

[7] Donald K, Paris PC. An evaluation of ΔK_{eff} estimation procedure on 6061-T6 and 2024-T3 aluminum alloys. Int J Fatigue 1999;21:S47–57.

[8] Walker EK. In: Effect of environment and complex load history on fatigue life. ASTM STP 462. American Society for Testing and Materials; 1970. p. 1–14.

[9] Dinda S, Kujawski D. Correlation and prediction of fatigue crack growth for different R-ratios using K_{max} and ΔK^+ parameters. Eng Fract Mech 2004;71:1779–90.

[10] Vasudevan AK, Sadanada K, Louat N. A review of crack closure, fatigue crack threshold and related phenomena. Mater Sci Eng A 1994;188:1–22.

[11] Noroozi AH, Glinka G, Lambert S. A two-parameter driving force for fatigue crack growth analysis. Int J Fatigue 2005;27:1277–96.

[12] Bowles CQ, Doctoral Dissertation, Delft University, The Netherlands; 1978.

[13] Zhang JZ. A shear band decohesion model for small fatigue crack growth in an ultra-fine grain aluminium alloy. Eng Fract Mech 2000;65:665–81.

[14] Sander M, Richard HA. Lifetime prediction for real loading situations-concepts and experimental results of fatigue crack growth. Int J Fatigue 2003;25:999–1005.

[15] Pommier S. A study of the relationship between variable level fatigue crack growth and the cyclic constitutive behavior of steel. Int J Fatigue 2001;23:S111–8.

[16] Landgraf RW, Morrow J, Endo T. Determination of the cyclic stress–strain curve. J Mater 1969;4(1):176.

[17] Technical report on low cycle fatigue properties of ferrous and non-ferrous materials. SAE Standard No. J1099. Warrendale (PA): Society of Automotive Engineers (SAE); 1998.

[18] Smith KN, Watson P, Topper TH. A stress–strain function for the fatigue of metals. J Mater 1970;5(4):767–78.

[19] Creager M, Paris PC. Elastic field equations for blunt cracks with reference to stress corrosion cracking. Int J Fract Mech 1967;3:247–52.

[20] Neuber H. Theory of stress concentration for shear-strained prismatic bodies with arbitrary nonlinear stress–strain law. Trans ASME J Appl Mech 1961;28:544–51.

[21] Glinka G, Buczynski A. In: Kalluri S et al., editors. Multi-axial fatigue and deformation. ASTM STP 1387. American Society for Testing and Materials; 2000. p. 82–98.

[22] Skrzypek JJ, Hetnarski RB. Plasticity and creep: theory, examples and problems. Boca Raton (FL): CRC Press; 1993.

[23] Bueckner HF. A novel principle for the computation of stress intensity factors. Z Angew Math Mech 1970;50:529–46.

[24] Glinka G, Shen G. Universal features of weight functions for cracks in Mode I. Eng Fract Mech 1991;40(6):1135–46.

[25] Shen G, Glinka G. Determination of weight functions from reference stress intensity factor. Theor Appl Fract Mech 1991;15:237–45.

[26] Wang X, Lambert S, Glinka G. Approximate weight functions for embedded elliptical cracks. Eng Fract Mech 1998;59:381–92.

[27] Kitagawa H, Takahashi S. Applicability of fracture mechanics to very small cracks in the early stage. In: Processing of the second international conference on mechanical behaviour of materials. Metals Park: American Society for Metals; 1976. p. 627–31.

[28] Pang C-M, Song J-H. Crack growth and closure behaviour of short fatigue cracks. Eng Fract Mech 1994;47(3):327–43.

[29] Liu AF. Structural life assessment methods. Materials Park (OH): ASM International; 1998.

[30] Wanhill RJH. Damage tolerance engineering property evaluation of aerospace aluminum alloys with emphasis on fatigue crack growth. In: National Research Laboratory NLR, Amsterdam, Technical Publication NLR TP 94177 U; 1994.

[31] Leis B. Cyclic inelastic deformation behaviour of thin notched plates, Master Thesis, University of Waterloo, Department of Civil Engineering; 1972.

[32] Dowling NE. Mechanical behaviour of materials. Englewood Cliffs (NJ): Prentice-Hall; 1999.

[33] Taylor DA. Compendium of fatigue threshold and growth rates. Warley, UK: EMAS Ltd.; 1985.

[34] Swain MH, Everett RA, Newman JC, Phillips EP. The growth of short cracks in 4340 steel and aluminum–lithium 2090. In: Edwards PR, Newman JC, editors. AGARD R-767; 1990. p. 7.1–7.30.

[35] Wanhill RJH. Private communication from Newman JC; 2005.

[36] Yuen A, Hopkins SW, Leverant GR, Rau CA. Correlations between fracture surface appearance and fracture mechanics parameters for stage II fatigue crack propagation in Ti–6Al–4V. Metall Trans 1974;5:1833–42.

[37] Ritchie RO, Boyce BL, Campbell JP, Roder O, Thompson AW, Milligan WW. Threshold for high-cycle fatigue in a turbine engine Ti–6Al–4V alloy. Int J Fatigue 1999;21:653–62.